Enhanced electromechanical coupling from cation local structures in (Mg,Zn)O

Junjun Jia [*]
Global Center for Science and Engineering (GCSE), Faculty of Science and Engineering, Waseda University, 3-4-1 Okubo, Shinjuku, Tokyo 169-8555, Japan

Daiki Kishi and Ningrui Bai
Graduate School of Advanced Science and Engineering, Waseda University, 3-4-1 Okubo, Shinjuku, Tokyo 169-8555, Japan

Toshihiko Okajima and Fabio Lesari
Aichi Synchrotron Radiation Center, Seto, Aichi 489-0965, Japan

Takahiko Yanagitani [†]
Graduate School of Advanced Science and Engineering, Waseda University, 3-4-1 Okubo, Shinjuku, Tokyo 169-8555, Japan; Kagami Memorial Research Institute for Materials Science and Technology, Waseda University, 2-8-26 Nishiwaseda, Tokyo 169-0051, Japan; and JST-CREST, 4-1-8 Honcho, Kawaguchi, Saitama 332-0012, Japan

(Received 27 October 2023; revised 6 February 2024; accepted 23 February 2024; published 1 April 2024)

Experimental measurements for the conversion loss between electric and mechanical energies of (Mg,Zn)O-based resonators show that Mg substitution can improve the electromechanical coupling of the wurtzite ZnO films up to the substitution concentration of 35%. Extended x-ray absorption fine structure (EXAFS) experiments indicate that both Mg and Zn exhibit tetrahedral local structures in (Mg,Zn)O films. With an increase in the Mg substitution concentration, the Zn-O bond length shows a slight tendency to increase and the Mg-O bond length practically remains the same. Further analysis of the EXAFS spectra reveals that a MgO_4 tetrahedron cluster exists in the oxide alloy. First-principles calculations reproduce the experimental results, suggesting that the enhanced electromechanical coupling is mainly attributed to a decrease in the dielectric constant due to the Mg substitution. The enhancement in piezoelectricity caused by Mg substitution originates from an increase in the Zn-O bond length along the *c* axis, which enhances the *c*-axis-oriented electric dipole moment. Furthermore, the calculations show that the Mg substitution can reduce the critical transition pressure from the wurtzite phase to the rocksalt phase. This study shows that combining the EXAFS experiment and theoretical calculation is a reliable method for understanding the relationship between the electromechanical coupling and local cation structure in wurtzite alloy systems. This can guide the search for novel piezoelectric materials.

DOI: 10.1103/PhysRevB.109.134101

I. INTRODUCTION

Wurtzite nitride alloys, such as (Sc,Al)N, exhibit an excellent electromechanical coupling effect with a high quality factor (Q) and thermal stability [1–3]. This has inspired their applications in electroacoustic devices, e.g., the film bulk acoustic resonator in microwave 5G communication. A well-established guideline for designing such wurtzite piezoelectric materials is to alloy the wurtzite nitride with a rocksalt-structured nitride to enhance the longitudinal piezoelectric constant and elastic softening of the host wurtzite nitride [4–7]. However, it is important to examine whether such a guideline is universal for the design of wurtzite piezoelectric ceramics, for example, by alloying the wurtzite oxide with a rocksalt oxide.

In a binary wurtzite structure ($P6_3mc$, space group 186), such as AlN, each cation is tetrahedrally coordinated with four anions, and vice versa, forming a corner-sharing tetrahedral structure. The center of the cation is displaced with respect to that of the anion along the *c* axis. This creates a *c*-axis-oriented electric dipole moment in each tetrahedral unit [8]. When a strain is applied along the *c* axis, the dipole moment is enhanced by the deformation of the tetrahedral unit, thereby generating a large piezoelectric response [9]. From the aspect of geometrical doping, owing to the noncentrosymmetric nature of the wurtzite structure, when a foreign atom has an ionic size close to that of host cation and is substituted into the cation site, the wurtzite structure can still maintain its piezoelectricity [7,10]. However, considering the interplay between a foreign atom and its local chemical environment, predicting the piezoelectricity of wurtzite alloys becomes challenging.

For AlN, the sp^3 hybridization between Al 3*s* and 3*p* and N 2*s* and 2*p* orbitals results in a local AlN_4 tetrahedral coordination. When Al is substituted by Sc, whose bonds to N are formed by Sc 3*d* and 4*s* orbitals, leading to an ScN_6 octahedral coordination in the cubic rocksalt phase, the Sc atom occupies a tetrahedral site instead of its favored octahedral sites [11]. This results in more displacement than Al

[*]jia@aoni.waseda.jp
[†]yanagitani@waseda.jp

 ©2024 American Physical Society

atoms from the regular tetrahedral positions, further forming a deformed tetrahedron. Such a local displacement causes a giant piezoelectric response with evident mechanical softening [4,11], and their synergy enhances the electromechanical coupling effect [3]. This is also observed in the (Yb,Al)N systems [7]. More experiments have shown that increasing the concentration of the substitutional element, such as Sc, Yb, or Cr in AlN [1,6,7], up to the composition-dependent phase boundary can rapidly improve the piezoelectric response.

Compared with the sp^3-hybridization induced tetrahedron in III–V wurtzite nitrides, the wurtzite oxide, ZnO, is considered to exhibit different microscopic formation mechanisms for local tetrahedron structures owing to the fully filled noninteracting $3d$ orbitals from the [Ar] $3d^{10}4s^2$ electronic configuration of Zn. According to the first-principles calculation, the formation of the ZnO_4 tetrahedral coordination was attributed to the intra-atomic $3d_{z^2}$-$4p_z$ orbital self-mixing of Zn, followed by an asymmetric hybridization between the Zn $3d_{z^2}$-$4p_z$ self-mixed orbital and O $2p_z$ orbital along the c axis, generating one short and one long bond along the c axis [8], which is considered as the origin of piezoelectricity. Alloying ZnO with cubic MgO has been reported to enhance the piezoelectric response of ZnO [12]. However, this enhancement is not evident compared with the (Sc,Al)N system [13]. Therefore, this necessitates a study of the origin of piezoelectricity in (Mg,Zn)O at the atomic level starting from a local cationic structure.

In addition to the enhanced piezoelectricity, cation substitution induces ferroelectricity in wurtzite alloys. Ferri *et al.* reported an enormous switchable polarization of >100 $\mu C/cm^2$ in $Mg_xZn_{1-x}O$ with x in the range between ∼30% and ∼37% and coercive fields below 3 MV/cm at room temperature, which encouraged the research on "ferroelectric everywhere" beyond the traditional perovskite-based materials [14]. The atomic-level mechanism for this polarization reversal is frequently conceptualized as the cation at the center of a tetrahedron switching to its symmetrical position along the basal plane, passing through a layered hexagonal phase under external electric field. Thus, understanding the local structure of cations in (Mg,Zn)O is also anticipated to contribute to elucidating polarization reversal in wurtzite materials.

To address the aforementioned questions, we investigated the local structures of cations in the (Mg,Zn)O alloy through extended x-ray absorption fine structure (EXAFS) experiments and measured the electromechanical coupling. Based on experimental observations, we conducted first-principles density functional theory (DFT) calculations to reveal the relationship between the local structures of cations and macroscopic electromechanical coupling, and examined the microscopic origin of the enhancement in piezoelectricity of the (Mg,Zn)O alloy.

II. EXPERIMENTAL AND COMPUTATIONAL DETAILS

The c-axis-oriented (Mg,Zn)O films with thicknesses of 5 to 10 μm were deposited on a (0001) Ti electrode film/silica glass substrate by radio frequency (RF) sputtering, which was used as a high-overtone bulk acoustic resonator (HBAR), where the sputtering targets were formed by pressing the mixture of MgO and ZnO powder (Furuuchi Chemical) with the varied molar ratio from $MgO/[MgO + ZnO] = 0.05$ to 0.55 with an interval size of 0.05. The Ar and O_2 gases were used as the sputtering gas and reactive gas, respectively, and their flow ratio (Ar/O_2) was 3. The RF sputtering power was 80 W, and the total gas pressure was set at 0.8 Pa. The distance between the target and the substrate was set to 48 mm. The electromechanical coupling coefficient (k_t^2) and the acoustic wave velocity (V_{33}^D) were determined by comparing the experimental and theoretical longitudinal wave conversion loss curves with the frequencies of the HBAR resonators [3]. The crystal structures of the (Mg,Zn)O film were characterized by x-ray diffraction (XRD) with using a Panalytical X'Pert Pro diffractometer in a 2θ-ω configuration with Cu Kα radiation ($\lambda \approx 1.5405$ Å). Scanning electron microscopy (SEM; JRD6500F) was used to characterize the cross-sectional morphology of the films, and the obtained Mg concentrations in the films were determined from the spectral intensities of energy-dispersive x-ray spectroscopy (EDS; JED2300F) [15], where the Mg concentration in the formed oxide alloy was defined as $x = Mg/[Mg + Zn]$. Further details can be found in Supplemental Material [16].

EXAFS measurements were conducted at beamlines BL1N2 and BL5S1 of the Aichi Light Source for the Mg K edge and Zn K edge, respectively. The Zn K-edge and Mg K-edge EXAFS spectra of the (Mg,Zn)O powders and the reference ZnO powder (standard crystalline powder from FUJIFILM Wako Pure Chemical Corporation) were recorded in the transmission and fluorescent yield modes, respectively. The (Mg,Zn)O powders were fabricated by scraping the (Mg,Zn)O sputtered films. All the measurements were performed at room temperature. The EXAFS data were processed and analyzed using the ATHENA and ARTEMIS codes [17]. After the spectra were extracted by removing the background using the Cook and Sayers method [18], the magnitudes of the Fourier transforms were obtained within the range of $k = 3.0$–8.2 Å^{-1} for the Mg and Zn K edges with the k^2 weighting of a Hanning window to obtain radial distribution functions. The data were fitted in the R space with fit ranges of $R = 1.0$–2.1 Å and $R = 1.0$–2.0 Å for the Mg K and Zn K edges, respectively.

For theoretical calculations, in order to model the random distribution of Mg atoms in the wurtzite (Mg,Zn)O structure, we first generated a $3 \times 3 \times 2$ supercell for the wurtzite ZnO, which consists of 36 Zn atoms and 36 O atoms. Then, a given number of Mg atoms were randomly substituted into Zn sites to form (Mg,Zn)O alloy with a composition x. For example, $x = 0.06$ means that two Mg atoms were randomly substituted into two of 36 Zn sites. For a given x, we generated ∼100 random structures in total, and then relaxed them to determine the lowest-energy configuration for further calculations by using the Vienna *ab initio* Simulation Package (VASP) [19,20] based on density functional theory [21]. The electronic exchange correlation interactions were treated by the generalized gradient approximation (GGA) in the parametrization scheme of Perdew, Burke, and Ernzerhof (PBE) [22]. A plane wave basis set with an energy cutoff of 450 eV and a Monkhorst-Pack k-point mesh of $3 \times 3 \times 3$ were used. The Gaussian smearing method with a 0.05 eV smearing width was used for the Brillouin-zone

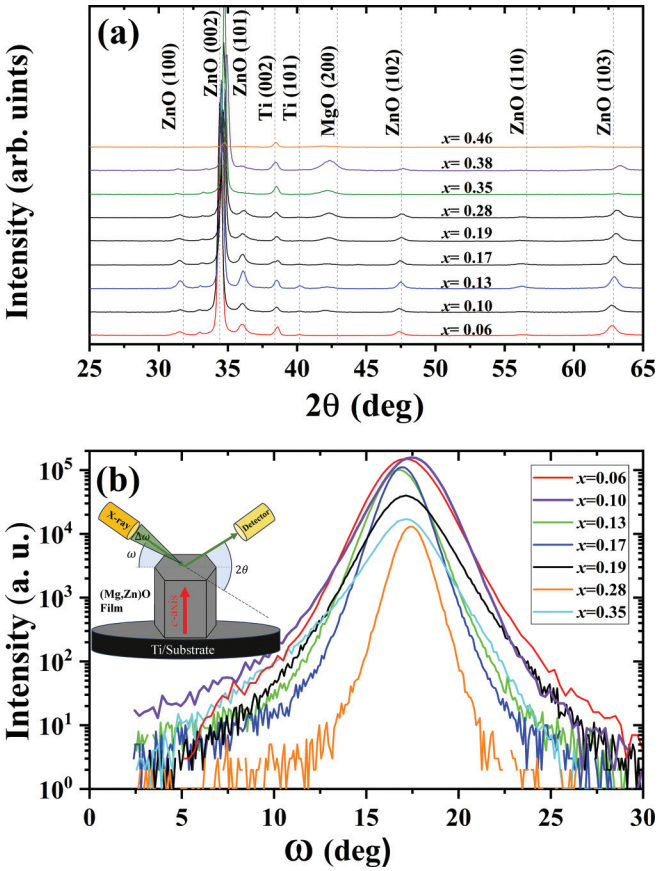

FIG. 1. (a) Diffraction pattern of (Mg,Zn)O films with different Mg concentrations, which were measured based on the $2\theta/\omega$ configuration. The Mg concentration of the formed oxide alloy is defined as $x = \mathrm{Mg}/[\mathrm{Mg} + \mathrm{Zn}]$. The dashed lines indicate the diffraction peaks of standard ZnO, MgO, and Ti powders [29–31]. (b) Rocking curves of (Mg,Zn)O films with different Mg concentrations, which were measured by ω scanning as indicated in the inset.

integration in the geometry optimization. The total energy for each random structure was converged to less than 10^{-6} eV. To understand the tendency of lattice spacing to change with Mg concentration in the wurtzite (Mg,Zn)O, we also relaxed the lowest-energy configurations by using the LDA functional, PBE functional with the Mg_{pv} potential (PBE-Mg_{pv}) [23], and PBE0 hybrid functional [24]. Moreover, the lowest-energy configuration was used to calculate the elastic and piezoelectric tensors using the density-functional perturbation theory [25–28], where a plane wave basis set with a cutoff energy of 450 eV was adopted after the cutoff test, and the total energy was converged to less than 10^{-8} eV. The Monkhorst-Pack k-point grids were set to $3 \times 3 \times 3$. Note that the Mg_{pv} potential with the p orbitals as valence orbitals is more accurate than the regular Mg potential [23].

III. RESULTS AND DISCUSSION

Structural characteristics. Figure 1(a) shows the $2\theta/\omega$ XRD patterns of the (Mg,Zn)O films at various Mg concentrations. The peaks observed around 31.52°, 34.46°, 36.08°, and 38.54° correspond to diffractions from the ZnO(100), ZnO(002), ZnO(101), and Ti(002) planes, respectively (JCPDS card no. 36-1451, 05-0682, 04-0829) [29–31]. For x below 0.38, the films exhibited high c orientation along the thickness direction [32]. Figure 1(b) shows the rocking curve of the ZnO(002) reflection by rotating the (Mg,Zn) film around the normal of the film. The FWHM widths of the rocking curves are less than 2.8°, confirming a high c orientation along the thickness direction. The introduction of MgO into ZnO resulted in a degradation in the film crystallinity. The peak around $2\theta = 42.38°$ became evident above $x = 0.19$, which was attributed to the diffraction from the MgO(200) plane [31]. Its broad FWHM suggested the presence of a nanocrystalline MgO phase in the film, which possibly relates to the Mg-related segregation or MgO precipitation on grain boundaries above a certain substitution concentration [33]. Based on the Scherrer formula, the MgO nanocrystallites were estimated to have medium-range correlations of a size scale of 8 nm at $x = 0.19$. Consequently, we conducted cross-sectional SEM observations with the EDS analysis to examine the distribution of Mg and Zn. The cross-sectional SEM image [Fig. 2(a)] reveals that the (Mg,Zn)O film at $x = 0.19$ has a polycrystalline nature with columnar structure, and compositional mapping on a selected area [Figs. 2(b)–2(d)] shows no noticeable pattern of Mg accumulation corresponding to the grain structure.

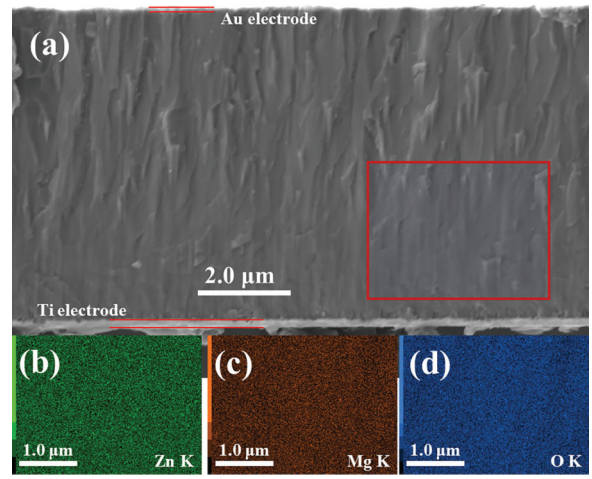

FIG. 2. (a) Cross-sectional SEM images at $x = 0.19$. (b)–(d) Compositional mappings for Zn, Mg, and O elements (Zn = green, Mg = red, O = blue) from the selected area (red rectangular).

The maximum incorporation concentration of Mg in (Mg,Zn)O was reported as $x = 0.17$, achieved through a solution-based growth method under approximate thermodynamic equilibrium conditions [33]. Considering the nonequilibrium nature of sputtering deposition, it is anticipated that the maximum incorporation concentration of Mg in (Mg,Zn)O can surpass that achieved by the solution-based growth method. This expectation arises from the fact that the supercooling of sputtered atoms on the substrate and a high deposition rate could kinetically limit the diffusion-controlled spinodal decomposition at high substitution concentrations [10]. This hypothesis of a larger maximum incorporation concentration in sputtered (Mg,Zn)O films can be examined by calculating the change of lattice spacing with the

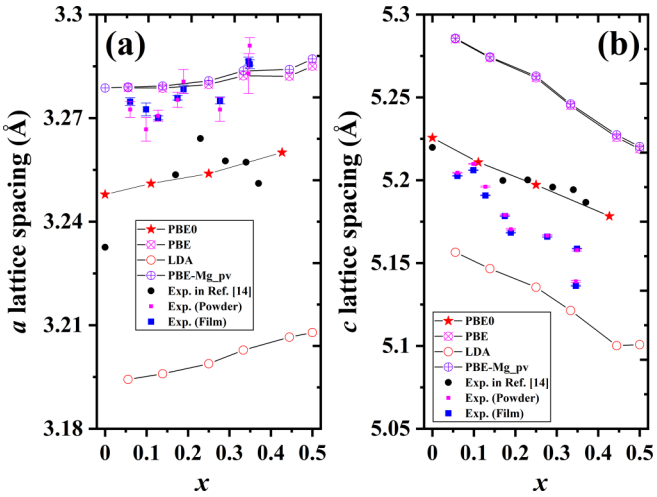

FIG. 3. The measured a (a) and c (b) lattice spacings are compared with those obtained from theoretical calculations using various functionals. The solid squares (blue) denote the measured lattice spacings from the XRD pattern of the (Mg,Zn)O films, while the solid squares (pink) represent the measured lattice spacings from the XRD pattern of the (Mg,Zn)O powder obtained by scraping the (Mg,Zn)O films. The black solid circles represent experimental data published in Ref. [14]. The remaining data points illustrate the calculated values using various functionals.

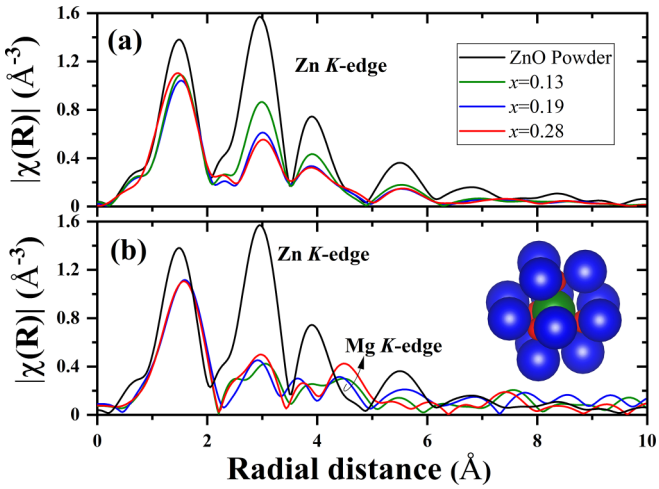

FIG. 4. FT EXAFS spectra measured without phase correction for the Zn K edge (a) and Mg K edge (b) in the (Mg,Zn)O films. The inset shows a schematic for the first and second EXAFS shells of the wurtzite structure (green: center atom; red: the first shell comprising four oxygen atoms; blue: the second shell comprising 12 Mg or Zn atoms).

substitution concentrations. Figure 1(a) shows that the ZnO(002) peak position exhibited an evident shift toward the high angle side with the Mg concentration up to $x \approx 0.35$, suggesting a decrease in the c-lattice spacing based on Bragg's law. Such a decrease is attributed to the substitution of Mg atoms with small ionic radius (0.57 Å) into the host Zn sites (ionic radius: 0.60 Å) up to $x \approx 0.35$ [34]. However, the ZnO(100) peak position almost remains constant, suggesting a constant a-lattice spacing with varied x, which seems contradictory to the observation in the c-lattice spacing. It is worth noting that the a- and c-lattice spacings derived from the XRD patterns of the (Mg,Zn)O films exhibit a close agreement with those obtained from the XRD patterns of (Mg,Zn)O powders, which were acquired by scraping the (Mg,Zn)O films, as shown in Fig. 3.

To elucidate the experimentally observed difference between a- and c-lattice spacings with x, we performed a series of structural optimization calculations to validate the variations in lattice spacing with x in wurtzite (Mg,Zn)O by using the LDA, PBE, and PBE-Mg_{pv} functionals, as well as PBE0 hybrid functionals. Figure 3 illustrates a comparison between the calculated a- and c-lattice spacings with the experimentally derived values from the XRD measurements. Additionally, the reported experimental values from another group [14] are also provided for comparison. The observed trend in the lattice constant to change with x is consistent with Ref. [14], and the difference can be attributed to the energetic bombardment during sputtering [14,35]. The LDA functional underestimates both a- and c-lattice spacings, as reported in other calculations [36]. The PBE0 functional also underestimates the a-lattice spacings, but gives the c-lattice spacings close to experimental values. In contrast, the a-lattice spacings with the PBE or PBE-Mg_{pv} potential are close to the experimental values, and the c-lattice spacings with PBE or PBE-Mg_{pv} functionals are larger than the experimental values. However, all the calculations using different functionals show the same trend with experimental observations; i.e., with an increase in x, the a-lattice spacing slightly increased, and the c-lattice spacing monotonically decreased. This agreement between our experimental and computational trends confirmed that Mg^{2+} can be substituted into the host Zn site up to $x \approx 0.35$ under nonequilibrium sputtering deposition.

Local structure of cations. The local structures of the cations (Mg and Zn) were investigated by EXAFS. Figure 4 shows the Fourier-transformed (FT) EXAFS spectra of the Zn and Mg K edges of the (Mg,Zn)O films and the standard ZnO powder, as a function of the interatomic distance. Compared with the EXAFS spectra of the standard ZnO power, the Zn local structures in the (Mg,Zn)O films were in a short-range order up to the fourth-nearest neighbor. On the other hand, the EXAFS spectral characteristics of the Mg K edge were similar to those of the Zn K edge up to the second-nearest neighbor, suggesting that Mg was substituted into the Zn site and had a local MgO_4 configuration. It is worth mentioning that although the MgO phase was observed in the (Mg,Zn)O film above $x = 0.17$, its content was considerably less because of the weak XRD intensity compared with that of the ZnO phase.

The bond length between the cation and anion in (Mg,Zn)O films was evaluated by first-shell EXAFS fittings. Indeed, instead of a MgO_6 octahedral structure in the cubic MgO, a MgO_4 tetrahedral structure can fit the EXAFS spectra well. Table I shows the bond lengths of the fitted Zn-O and Mg-O. The Zn-O bond length shows a slight tendency to increase with x up to 0.19. In comparison, the Mg-O bond length almost remains unchanged, suggesting a stable MgO_4 tetrahedral structure without a change in x.

TABLE I. Bond lengths of Zn-O and Mg-O in the (Mg,Zn)O films, evaluated by the first-shell EXAFS fittings. Here, r is the phase-corrected interatomic distance in units of Å, and DW is the Debye-Waller factor in units of Å^2.

	Zn-O bond		Mg-O bond	
	r	DW ($\times 10^{-3}$)	r	DW ($\times 10^{-3}$)
ZnO	1.95(4)	5.2(29)	–	–
$x = 0.13$	1.97(4)	8.9(56)	1.98(1)	7.4(8)
$x = 0.19$	1.98(8)	9.9(49)	1.99(2)	7.7(11)
$x = 0.28$	1.95(1)	8.6(7)	1.99(1)	7.3(9)

In addition to the bond length, the EXAFS spectra provide the information regarding the coordination number. From the crystallographic perspective, the atoms are arranged with a tetrahedral symmetry in a binary wurtzite structure; i.e., any one cation (anion) has four first-nearest-neighbor anions (cations) and 12 second-nearest-neighbor cations (anions). For the investigated wurtzite structured oxide alloy systems, the only difference between the cationic and anionic sublattices is that, for the anionic sublattice, 12 atoms around each O atom are O atoms, but for the cationic sublattice both Zn and Mg atoms are present around any Zn or Mg atom [37]. As shown in Fig. 4, the first peak around 1.8 Å corresponds to four first-nearest oxygen atoms, and the second peak around 3.0 Å is associated with 12 second-nearest Mg and/or Zn atoms. For the Mg K-edge spectra, the first peak almost remains the same, and the peak position of the second shell shifts with x, suggesting a change in the cation type and number with x. This further suggests the formation of a MgO_4 cluster with a short-range order in the (Mg,Zn)O alloy.

Electromechanical coupling. The LDA and PBE-Mg$_{pv}$ functionals were used to calculate the electromechanical coupling coefficients of (Mg,Zn)O. Theoretically, the experimentally measured k_t^2 can be compared with the calculated k_{33}^2 based on $k_t^2 \sim k_{33}^2 = e_{33}^2/\epsilon_{33}c_{33}$, where e_{33}, ϵ_{33}, and c_{33} are the piezoelectric, dielectric, and elastic constants, respectively [7,38]. Figure 5(a) shows that the k_{33}^2 values with PBE-Mg$_{pv}$ reproduced the experiments for k_t^2 up to approximately $x \sim 0.35$. In the experiments, k_t^2 exhibited a tendency to increase with x up to 0.35, and the maximal k_t^2 was 9.61% at $x = 0.32$, as shown in Fig. 5(a). This result corresponded with a reduction in d_{33} above $x > 0.35$, as reported by Kang *et al.* [12].

Moreover, V_{33}^D was measured by using acoustic wave resonance spectra [39]. As shown in Fig. 5(b), the calculated V_{33} exhibited a similar tendency with experimentally measured V_{33}^D with x up to 0.19, which is a synergistic effect due to the decrease of both c_{33} and the film density. However, V_{33}^D rapidly decreased above $x = 0.35$ as k_t^2 did. Such a destruction in electromechanical coupling or piezoelectricity should be attributed to the phase separation of cubic MgO and wurtzite ZnO phases due to the thermodynamic driving force, as revealed by the XRD pattern in Fig. 1(a). Herein, $x = 0.35$ was considered as the critical point of structural stability for the wurtzite phase [12].

Based on the quantitative agreement between the calculation and experimental results up to $x = 0.25$, we investigated the microscopic mechanism of the change in k_t^2 with the Mg concentration. Table II lists the calculated dielectric constants, piezoelectric constants, and elastic moduli for (Mg,Zn)O with different x compared with the experiments [40–42]. With an increase in x up to 0.25, ϵ_{33} decreased by 30% from 14.24 to 9.85, c_{33} slightly decreased by 9% from 247 to 224 GPa, and e_{33} increased by 9% from 1.11 to 1.21 C/m^2. For ϵ_{33}, experimental measurements indicate that it decreases from ~12.6 in ZnO to 9.5 in (Mg,Zn)O with $x = 0.35$ [12,40,43], which is almost consistent with the present calculations. Following $k_t^2 \sim e_{33}^2/\epsilon_{33}c_{33}$, a 30% decrease in ϵ_{33} was considered to dominate the increase in k_t^2 together with mechanical softening and enhanced piezoelectricity.

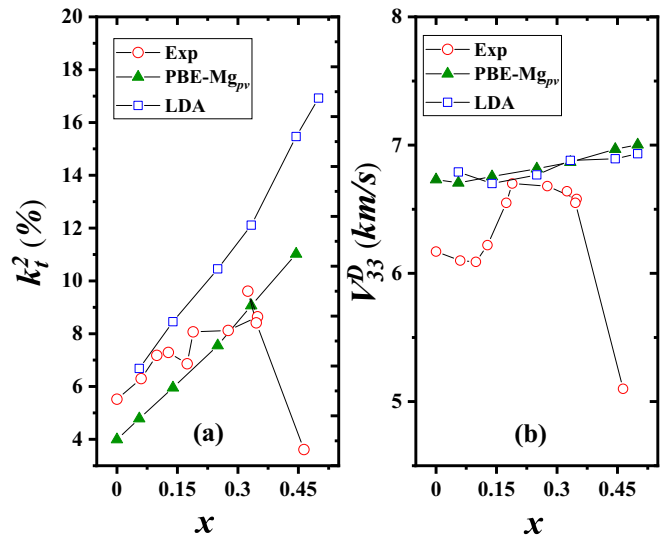

FIG. 5. Calculated k_{33}^2 (a) and V_{33} (b) values compared with the experimentally determined k_t^2 and V_{33}^D for the (Mg,Zn)O films, respectively. The squares and triangles represent the calculated k_{33}^2 using the LDA and PBE-Mg$_{pv}$ functionals, respectively. The circles indicate the measured k_t^2.

Mechanical softening. Table II shows that as x increases from 0.00 to 0.50, c_{33} decreases from 247 to 216 GPa, indicating mechanical softening in (Mg,Zn)O. For ZnO, the PBE functional generally overestimates c_{33} compared to the experimental values [44]. The present calculation shows that the PBE-Mg$_{pv}$ functional is 17% higher than the experimental value for ZnO. Due to the lack of experimental data for c_{33} in (Mg,Zn)O, it is challenging to directly compare the calculated c_{33} with the experiments. However, V_{33} calculated from c_{33} and the density ρ of (Mg,Zn)O based on $V_{33} = c_{33}/\rho$ is in agreement with the measured V_{33}^D, especially for (Mg,Zn)O with x ranging from 0.17 to 0.35. Compared with the evident mechanical softening from 368.2 GPa in AlN to 131.8 GPa in $Al_{0.5}Sc_{0.5}N$ [4], introducing MgO into ZnO only gave rise to a slight decrease in c_{33}.

Intuitively, when the packing is much denser in the c direction of the wurtzite structure, the material should be significantly harder in this direction [45]. This holds for (Sc,Al)N or (Yb,Al)N since their c_{33} decreases as the c lattice spacing increases. However, for the (Mg,Zn)O system, when the c lattice spacing decreases with an increase in x, c_{33} decreases. Such a difference between (Sc,Al)N and (Mg,Zn)O can be understood as a superposition of the geometrical effect of cation

TABLE II. Dielectric (ϵ_{33}), elastic (c_{ij}), and piezoelectric (e_{ij}) constants as well as electromechanical coupling coefficient (k_{33}) of (Mg,Zn)O at varied x, where ϵ_{33} is the 33 component of the dielectric tensor. Elastic and piezoelectric constants are expressed in GPa and C/m^2, respectively. The measured c_{ij} and e_{ij} values for ZnO from other groups were provided for comparison.

	ϵ_{33}	c_{11}	c_{12}	c_{13}	c_{33}	c_{44}	e_{31}	e_{33}	k_{33}^2 (%)
Computational results in this study:									
$x = 0.00$ (ZnO)	14.24	195	104	107	247	43	−0.58	1.11	3.99
$x = 0.06$	12.51	194	104	103	240	44	−0.58	1.13	4.78
$x = 0.14$	11.00	196	104	102	233	45	−0.58	1.16	5.62
$x = 0.25$	9.85	203	108	102	224	47	−0.58	1.21	7.02
$x = 0.33$	9.19	208	110	101	216	48	−0.58	1.26	9.07
$x = 0.44$	8.58	213	112	102	208	51	−0.59	1.32	11.02
$x = 0.50$	8.21	216	113	102	203	52	−0.63	1.43	13.88
Experimental results from other groups:									
ZnO	9.2–12.6[a]	210[b]	121[b]	105[b]	211[b]	42[b]	–	1.32[c]	–
(Mg,Zn)O ($x = 0.25$)	10.3[d]	–	–	–	–	–	–	–	–

[a]Polycrystalline thin films fabricated by RF sputtering [40], and the static dielectric constant for ZnO nanoparticle is ∼13.0 [43].
[b]ZnO single crystals measured using the ultrasonic pulse technique [41].
[c]Reference [42].
[d]Moreover, $\epsilon_{33} = 9.6$ at $x = 0.30$ and $\epsilon_{33} = 9.5$ at $x = 0.35$ from Ref. [12].

substitution and chemical interactions between substitutional and host atoms. From the geometrical aspect, a smaller ionic size of Mg^{2+} compared with that of Zn^{2+} gave rise to a decrease in the c lattice spacing, which is expected to lead to mechanical hardening. Therefore, the interatomic interactions between the substitutional Mg and its local chemical environment should have dominated the mechanical softening.

Enhanced piezoelectricity. Table II shows that e_{33} increased by 9% from 1.11 to 1.21 C/m^2 with an increasing in x from 0.00 to 0.25. Such a weak dependence on the Mg concentration for the piezoelectric response in (Mg,Zn)O is also confirmed by the first-principles calculations with the PBE0 hybrid functional [13]. Microscopically, e_{33} can be divided into two main contributions: (1) an electronic response to the strain of the crystal structure (clamped-ion term) and (2) the effect of internal strain on piezoelectric polarization [46], which is formulated as follows:

$$e_{33}(x) = e_{33}^{\text{clamped-ion}}(x) + \frac{4eZ_{33}(x)}{\sqrt{3}a(x)^2}\frac{du}{d\sigma}, \tag{1}$$

where e is the elementary charge, a represents the equilibrium lattice parameter, Z represents the dynamical Born or transverse charge in units of e, σ is the macroscopic applied strain, and u is the wurtzite internal parameter defined as the anion-cation bond length along the (0001) axis in units of the c-lattice spacing. As shown in Fig. 6(a), a monotonic increase was observed for the clamped-ion term. In comparison, the second term, representing the strain-induced piezoelectric contribution, practically remained unchanged with x in Fig. 6(b). Thus, an increased piezoelectric response was considered from the clamped-ion term. Note that the enhanced piezoelectric response in the well-established (Sc,Al)N [4] or (Yb,Al)N [7] is mainly dominated by the effect of internal strain, as shown by the comparison between (Yb,Al)N and (Mg,Zn)O in Fig. 6.

To reveal the physical mechanism of the enhanced e_{33}, we examined the local structure of the Mg and Zn atoms in the (Mg,Zn)O alloy, which were fixed in the calculation. In the ideal ZnO structure, the apical and basal Zn-O bond lengths were 2.005 and 1.998 Å, respectively, where apical and basal oxygens are depicted in Fig. 7(a). Table III shows that the basal Zn-O bond lengths almost remained the same at different substitution concentrations. This suggested that the local distortions were not evident on the basal plane of wurtzite (Mg,Zn)O, as shown by the dispersion of the legs of the tetrahedral bonds in Fig. 7(b). This differed from the clear local structural distortions on the basal plane in the well-studied (Sc,Al)N [2] or the relaxed (Yb,Al)N shown in the inset of Fig. 7(b). These observations were confirmed by further calculations regarding the bond angles between the basal Zn-O bonds or between the basal Mg-O bonds. Even when more Mg was substituted, the bond angle slightly varied from 108.82° to 107.93° between the basal Zn-O bonds, and changed from 109.94° to 110.53° between the basal Mg-O bonds. This suggested that the enhanced piezoelectric

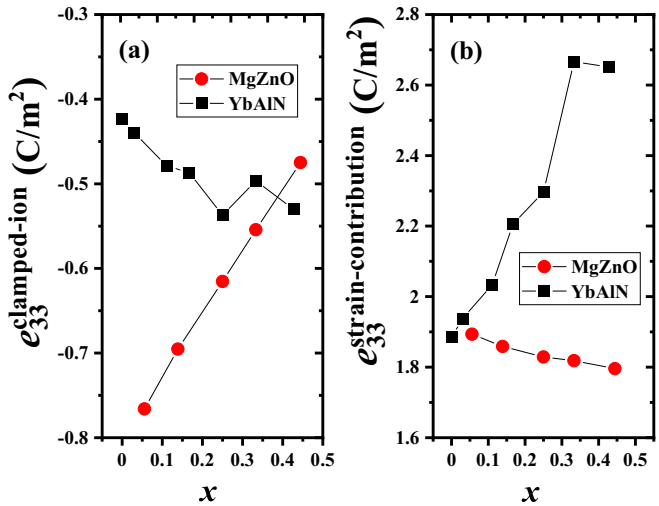

FIG. 6. Calculated contributions of e_{33} introduced in Eq. (1). (a) Clamped-ion contribution. (b) Internal strain contribution. The black squares are calculation results data taken from Ref. [7].

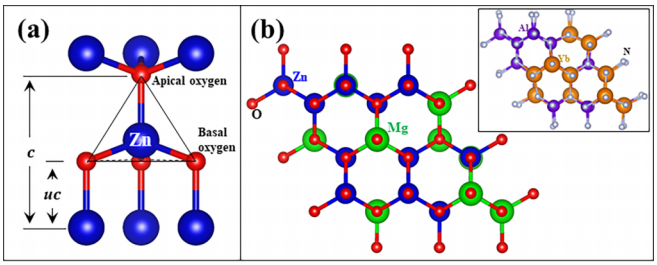

FIG. 7. (a) Local tetrahedral environment of cations in the wurtzite structure. The definitions of apical and basal oxygen atoms in the local structure are given. (b) Relaxed (Mg,Zn)O structure ($x = 0.33$), and the inset shows evident local structural distortions around the cations in the relaxed (Yb,Al)N structure with Yb/[Yb + Al] = 0.33, which was obtained by DFT calculation with the PBE functional using the same calculation procedures as described in Sec. II.

response was not due to the deformed tetrahedron as that in (Sc,Al)N [11].

On the other hand, the apical tetrahedral bond length increased with x in tetrahedral ZnO_4, as shown in Table III. It is expected to improve the bond polarization along the c axis, thereby increasing the piezoelectric response. In comparison, Table III shows that the calculated bond lengths for the tetrahedral MgO_4 almost remained constant, which was consistent with the EXAFS observations as shown by the first peaks in Fig. 4(b). In addition to the bond lengths, the bond angle between the basal Mg-O bonds, or the bond angle between the apical and basal Mg-O bonds, slightly changed within 0.5°. These results suggested that the MgO_4 tetrahedral configuration was fairly stable at a varied x. Taking all into account, the enhanced piezoelectric response was considered to mainly originate from the increased apical Zn-O bond along the c axis, which enhanced the c-axis-oriented electric dipole moment in each tetrahedral unit, leading to an increase in the piezoelectric coefficient.

Composition-driven morphotropic phase boundary. For piezoelectric materials, morphotropic phase boundaries (MPBs) represent a transition region in the phase diagram in the vicinity of which crystal structures become highly susceptible to external stimuli [47]. Under external stimulus, piezoelectric films can be reversibly transformed between

TABLE III. Local structural parameters (apical and basal Zn-O bonds) of (Mg,Zn)O with different x from first-principles calculations, where the Mg_{pv} potential was used.

			Zn-O (Å)		Mg-O (Å)	
	a (Å)	c (Å)	Apical	Basal	Apical	Basal
ZnO	3.2859	5.3034	2.005	1.998	–	–
$x = 0.06$	3.2787	5.2851	2.006	1.998	1.991	1.982
$x = 0.14$	3.2793	5.2749	2.007	1.999	1.991	1.982
$x = 0.25$	3.2807	5.2629	2.009	1.999	1.989	1.983
$x = 0.33$	3.2835	5.2465	2.010	2.000	1.993	1.981
$x = 0.44$	3.2836	5.2289	2.012	2.001	1.994	1.982
$x = 0.50$	3.2867	5.2212	2.016	2.001	1.992	1.982

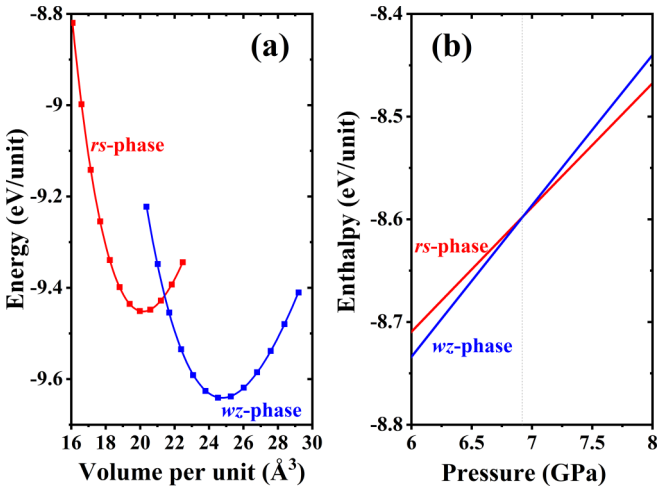

FIG. 8. (a) Total energy-volume curves calculated for the rocksalt and wurtzite (Mg,Zn)O phases at $x = 0.25$. The scattered points are the calculated total energies at the give volume, and the solid lines are the Birch-Murnaghan fitting curves. (b) Critical phase transition pressure determined from the enthalpy versus pressure plot. Note that the "unit" refers to one "cation-oxygen" formula unit present in the corresponding phases. Full details for the calculations can be found in Supplemental Material [53] (see also Refs. [11,13,15,17,18] therein).

competing structural polymorphs due to their similar free energies in a flattened free-energy landscape, as revealed in (Sc,Al)N through first-principles calculations [4]. Significant enhancements in the electromechanical properties have been observed in piezoelectric materials near the MPBs [48], such as (Sc,Al)N films [1,3]. Tailoring MPBs to achieve high piezoelectric response has been described for composition-driven morphotropic systems [49]. Considering a possible transformation from the wurtzite to rocksalt (Mg,Zn)O phase as implied in Fig. 1(a), we further investigate the phase boundary between wurtzite and rocksalt (Mg,Zn)O to understand the enhanced k_t^2 observed in experiments.

Figure 8(a) shows that the total energy of the wurtzite and rocksalt (Mg,Zn)O phases was calculated as a function of the unit volume, where the unit refers to one "cation-oxygen" formula unit present in the corresponding rocksalt and wurtzite phase. The calculated total energies were fitted to the Birch-Murnaghan equation of state to determine the structural parameters [50–52]. Such total energy-volume curves can provide an indication of which of the structures are the best candidate as the more stable phase. Generally, the structure with the lowest equilibrium energy is considered to be the more stable phase. Thus, the wurtzite phase is considered more stable than the rocksalt phase at $x = 0.25$. However, the difference between the lowest equilibrium energies of wurtzite and rocksalt (Mg,Zn)O decreases with x increasing, as seen in Supplemental Material [53], implying the existence of the phase boundary between the wurtzite to rocksalt phases. As discussed above, our sputtering experiments indicate that (Mg,Zn)O films exhibit a composition-driven phase boundary between wurtzite and rocksalt phases around $x \sim 0.35$. This further suggests that the maximal k_{33}^2 around $x = 0.35$ observed in the experiments was possibly related to

the composition-driven MPBs phenomenon owing to the alloy physics of the wurtzite (Mg,Zn)O phase, which generates a piezoelectric response to an external mechanical strain (and vice versa).

Further calculation for the pressure-enthalpy relation [54,55] indicates that (Mg,Zn)O at $x = 0.25$ undergoes a structural phase transition from the wurtzite to rocksalt phases around 6.9 GPa, as can be seen from Fig. 8(b). This critical pressure is below 11.1 GPa of pure ZnO [56–58], which was calculated using the same procedure and closely corresponded with the reported experimental values of 8.7 GPa [59], 9.0 GPa [60], and 10.1 GPa [61]. Note that the present PBE result (11.1 GPa) is well in agreement with other PBE values of 11.51 GPa [62] and 11.8 GPa [63] from other groups. Therefore, substituting Mg atoms into ZnO is considered to lead to a decrease in the critical pressure. This deduction is consistent with the experimental observation that the single rocksalt (Mg,Zn)O with any compositions is observed when the external pressure is $\geqslant$6.5 GPa [64]. Moreover, Seko *et al.* employed the cluster expansion and cluster variation method to calculate the phase diagram of the ZnO-MgO system [65], and drew a similar conclusion. See more details about the composition dependence of critical pressure in Supplemental Material [53]. This fact, that the critical pressure can be adjusted by chemical composition of (Mg,Zn)O, opens new perspectives for designing novel wurtzite piezoelectric alloys with tunable piezoelectric response and thus an electromechanical coupling response driven by the external pressure.

MgO_4 *tetrahedron in* (Mg,Zn)O. The EXAFS experiments confirmed the presence of a tetrahedral MgO_4 local structure in the (Mg,Zn)O films. They indicated that the bond length of the average first-nearest neighbor did not change with x. The DFT calculations reproduced the experiments, suggesting that MgO_4 had a stable configuration at different x values, where three bond lengths on the *ab* plane and one bond length along the c axis almost remained constant at varied x values. Thus, a question arises as to why the MgO_4 tetrahedron is stable at different x values.

From the aspect of orbital interaction, the covalent-bonding interaction between Zn $3d$ and O $2p$ orbitals has been proposed as a cause of piezoelectricity [66]. However, the fully filled Zn $3d$ orbitals were considered not capable of forming hybridized orbitals with the axial O $2p_z$ orbitals. A new bonding mechanism responsible for triggering piezoelectricity in the wurtzite ZnO was attributed to a self-mixing of Zn $3d_{z^2}$ and Zn $4p_z$ orbitals [8], as shown in Fig. 9(a). Such mixing resulted in an orbital characterized by an asymmetric shape along the c axis and generated one short and one long bond along the c axis, which was considered as the microscopic origin of ZnO piezoelectricity. Conversely, Mg has a [Ne] $3s^2$ electronic configuration, and thus lacks the hybridization between d and p orbitals. This removes the possibility of forming a tetrahedral MgO_4 coordination, as in ZnO. Here, the sp^3 hybridization between Mg $3s$, $2p$ and O $2p$ was considered to generate a local MgO_4 tetrahedral coordination, as shown by the states around 1.5 eV below the Fermi level in Fig. 9(b). Moreover, the Mg p_z states were slightly higher than its p_x and p_y states, implying that the apical bond length along the

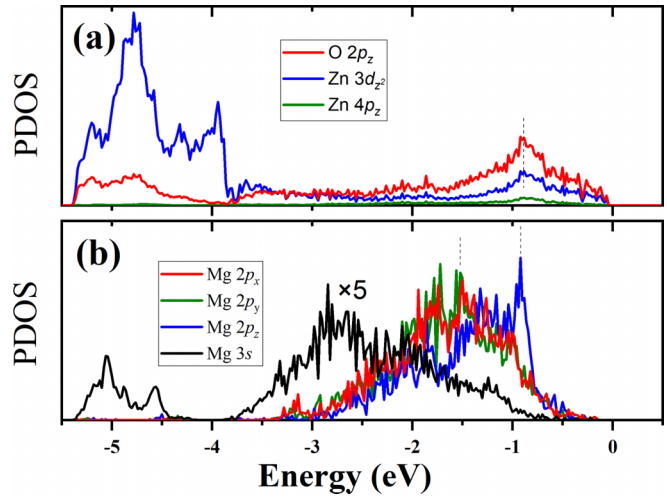

FIG. 9. (a) Projected density of states (PDOS) in wurtzite (Mg,Zn)O with $x = 0.33$ calculated from PBE calculations. The dashed line shows the mixing of Zn $3d_{z^2}$ and Zn $4p_z$ orbitals interacting with the O $2p_z$ orbital. (b) PDOS of Mg in wurtzite (Mg,Zn)O alloy. The Fermi level is set to 0.

c axis was longer than ones on the basal plane in tetrahedral MgO_4.

Noteworthily, MgO was reported to be unstable to maintain the wurtzite structure under ambient pressure [67], and its stable phase was rocksalt with the MgO_6 local structure. Contrarily, our EXAFS experiments suggested a stable MgO_4 local structure in the sputtered (Mg,Zn)O films, as revealed by the EXAFS spectra shown in Fig. 4(b). This may be associated with the spatial distribution of MgO_4 tetrahedrons in the (Mg,Zn)O solid solution. The DFT calculations revealed the existence of a MgO_4 cluster in the relaxed alloy structure beginning from $x = 0.14$, as revealed by EXAFS experiments. In addition, the states related to Mg p_x and p_y orbitals were approximately 0.5 eV lower than the Zn-O bonding states. This implied that the MgO_4 tetrahedron was more stable than the ZnO_4 tetrahedron in the (Mg,Zn)O alloy, originating from the fact that MgO has considerably stronger ionic bonds than ZnO [13].

IV. CONCLUSIONS

The experiments showed that alloying cubic MgO into wurtzite ZnO enhanced the electromechanical coupling, where k_t^2 is improved from 5.52% to 9.61%. Based on the EXAFS measurements, Mg was considered to be substituted into the Zn sites in the wurtzite ZnO structure. Moreover, fitting the EXAFS spectra indicated an increased Zn-O bond length and an unchanged Mg-O bond length at up to 25% Mg substitution concentration. The DFT calculations agree well with the experiments, including the tendency of k_t^2 and the bond length with the Mg substitution, suggesting that the enhanced electromechanical coupling was dominated by a decrease in the dielectric constant due to Mg substitution. Compared with the Sc substitution in AlN, which produced a deformed tetrahedron and thus a giant increase in piezoelectricity, the Mg substitution in ZnO only slightly enhanced the

e_{33} of (Mg,Zn)O. This was because although the Mg substitution induced an increased Zn-O bond length along the c axis, it had a low influence on the tetrahedral configuration, such as the bond angles. Moreover, the calculations indicated that the Mg substitution in ZnO lowers the critical transition pressure from the wurtzite to rocksalt phases. The critical transition pressure is reduced from 11.1 GPa for ZnO to 6.9 GPa for (Mg,Zn)O with $x = 0.25$.

Overall, the EXAFS experiments can provide reliable information on the local structure of constituent elements in the wurtzite alloy, enabling us understand the dispersion of substitutional elements in the host material and the microscopic origin of piezoelectricity. Combining EXAFS experiments and theoretical calculation also represents a reliable approach for understanding alloy-based piezoelectric materials, advancing the research on novel piezoelectric materials.

ACKNOWLEDGMENTS

J.J. acknowledges funding from a JSPS KAKENHI Grant-in-Aid for Scientific Research (C) (Grant No. 20K05368) and from the Waseda University Grant for Special Research Projects (Projects No. 2023C-169 and No. 2023Q-013). T.Y. is grateful for support from JST CREST (Grant No. JPMJCR20Q1), JST FOREST (Grant No. JPMJFR212L), and JST A-STEP (Grant No. JPMJTR231C), Japan. The computation in this research was conducted using the Fujitsu PRIMERGY CX400M1/CX2550M5 (Oakbridge-CX) at the Information Technology Center, University of Tokyo. The EXAFS experiments were conducted at the BL1N2 and BL5S1 of Aichi Synchrotron Radiation Center, Aichi Science and Technology Foundation, Aichi, Japan (Proposals No. 202302008 and No. 202302048).

[1] M. Akiyama, T. Kamohara, K. Kano, A. Teshigahara, Y. Takeuchi, and N. Kawahara, Enhancement of piezoelectric response in scandium aluminum nitride alloy thin films prepared by dual reactive cosputtering, Adv. Mater. **21**, 593 (2009).

[2] C. Tholander, I. A. Abrikosov, L. Hultman, and F. Tasnádi, Volume matching condition to establish the enhanced piezoelectricity in ternary $(Sc,Y)_{0.5}(Al,Ga,In)_{0.5}N$ alloys, Phys. Rev. B **87**, 094107 (2013).

[3] T. Yanagitani and M. Suzuki, Enhanced piezoelectricity in Yb-GaN films near phase boundary, Appl. Phys. Lett. **104**, 082911 (2014).

[4] F. Tasnádi, B. Alling, C. Hoglund, G. Wingqvist, J. Birch, L. Hultman, and I. A. Abrikosov, Origin of the anomalous piezoelectric response in wurtzite $Sc_xAl_{1-x}N$ alloys, Phys. Rev. Lett. **104**, 137601 (2010).

[5] C. Tholander, F. Tasnádi, I. A. Abrikosov, L. Hultman, J. Birch, and B. Alling, Large piezoelectric response of quarternary wurtzite nitride alloys and its physical origin from first principles, Phys. Rev. B **92**, 174119 (2015).

[6] S. Manna, K. R. Talley, P. Gorai, J. Mangum, A. Zakutayev, G. L. Brennecka, V. Stevanović, and C. V. Ciobanu, Enhanced piezoelectric response of AlN via CrN alloying, Phys. Rev. Appl. **9**, 034026 (2018).

[7] J. Jia and T. Yanagitani, Origin of enhanced electromechanical coupling in (Yb,Al)N nitride alloys, Phys. Rev. Appl. **16**, 044009 (2021).

[8] J.-H. Lee, W.-J. Lee, S.-H. Lee, S. M. Kim, S. Kim, and H. M. Jang, Atomic-scale origin of piezoelectricity in wurtzite ZnO, Phys. Chem. Chem. Phys. **17**, 7857 (2015).

[9] S. Roberts, Dielectric and piezoelectric properties of barium titanate, Phys. Rev. **71**, 890 (1947).

[10] J. Jia, N. Iwata, M. Suzuki, and T. Yanagitani, Enhanced electromechanical coupling in Yb-substituted III–V nitride alloys, ACS Appl. Electron. Mater. **4**, 3448 (2022).

[11] D. F. Urban, O. Ambacher, and C. Elsässer, First-principles calculation of electroacoustic properties of wurtzite (Al,Sc)N, Phys. Rev. B **103**, 115204 (2021).

[12] X. Kang, S. Shetty, L. Garten, J. F. Ihlefeld, S. Trolier-McKinstry, and J. P. Maria, Enhanced dielectric and piezoelectric responses in $Zn_{1-x}Mg_xO$ thin films near the phase separation boundary, Appl. Phys. Lett. **110**, 042903 (2017).

[13] J. Huang, Y. Hu, and S. Liu, Origin of ferroelectricity in magnesium-doped zinc oxide, Phys. Rev. B **106**, 144106 (2022).

[14] K. Ferri, S. Bachu, W. Zhu, M. Imperatore, J. Hayden, N. Alem, N. Giebink, S. Trolier-McKinstry, and J.-P. Maria, Ferroelectrics everywhere: Ferroelectricity in magnesium substituted zinc oxide thin films, J. Appl. Phys. **130**, 044101 (2021).

[15] M. F. Gazulla, M. Rodrigo, E. Blasco, and M. Orduña, Nitrogen determination by SEM-EDS and elemental analysis, X-Ray Spectrom. **42**, 394 (2013).

[16] See Supplemental Material at http://link.aps.org/supplemental/10.1103/PhysRevB.109.134101 for additional information on the determination of Mg concentration in (Mg,Zn)O films, which includes Ref. [15].

[17] B. Ravel and M. Newville, Athena, Artemis, Hephaestus: Data analysis for x-ray absorption spectroscopy using IFEFFIT, J. Synchrotron Radiat. **12**, 537 (2005).

[18] J. Jia, A. Suko, Y. Shigesato, T. Okajima, K. Inoue, and H. Hosomi, Evolution of defect structures and deep subgap states during annealing of amorphous In-Ga-Zn oxide for thin film transistors, Phys. Rev. Appl. **9**, 014018 (2018).

[19] G. Kresse and J. Hafner, *Ab initio* molecular dynamics for liquid metals, Phys. Rev. B **47**, 558 (1993).

[20] G. Kresse and J. Hafner, Norm-conserving and ultrasoft pseudopotentials for first-row and transition elements, J. Phys.: Condens. Matter **6**, 8245 (1994).

[21] P. Hohenberg and W. Kohn, Inhomogeneous electron gas, Phys. Rev. **136**, B864 (1964).

[22] J. P. Perdew, K. Burke, and M. Ernzerhof, Generalized gradient approximation made simple, Phys. Rev. Lett. **77**, 3865 (1996).

[23] M. Rang and G. Kresse, First-principles study of the melting temperature of MgO, Phys. Rev. B **99**, 184103 (2019).

[24] J. P. Perdew, M. Ernzerhof, and K. Burke, Rationale for mixing exact exchange with density functional approximations, J. Chem. Phys. **105**, 9982 (1996).

[25] D. Vanderbilt, Berry-phase theory of proper piezoelectric response, J. Phys. Chem. Solids **61**, 147 (2000).

[26] X. Gonze and C. Lee, Dynamical matrices, Born effective charges, dielectric permittivity tensors, and interatomic force constants from density-functional perturbation theory, Phys. Rev. B **55**, 10355 (1997).

[27] X. Wu, D. Vanderbilt, and D. R. Hamann, Systematic treatment of displacements, strains, and electric fields in density-functional perturbation theory, Phys. Rev. B **72**, 035105 (2005).

[28] R. D. King-Smith and D. Vanderbilt, Theory of polarization of crystalline solids, Phys. Rev. B **47**, 1651 (1993).

[29] JCPDS–International Centre for Diffraction Data No. 36-1451 (1996).

[30] H. E. Swanson, R. K. Fuyat, and G. M. Ugrinic, Natl. Bur. Stand. Circ. 539, **III** (1954).

[31] H. E. Swanson, and E. Tatge, Natl. Bur. Stand. Circ. 539, **I** (1953).

[32] J. Jia, A. Takasaki, N. Oka, and Y. Shigesato, Experimental observation on the Fermi level shift in polycrystalline Al-doped ZnO films, J. Phys. Appl. **112**, 013718 (2012).

[33] M. K. Yadav, M. Ghosh, R. Biswas, A. K. Raychaudhuri, A. Mookerjee, and S. Datta, Band-gap variation in Mg- and Cd-doped ZnO nanostructures and molecular clusters, Phys. Rev. B **76**, 195450 (2007).

[34] R. D. Shannon, Revised effective ionic radii and systematic studies of interatomic distances in halides and chalcogenides, Acta Crystallogr. A **32**, 751 (1976).

[35] J. Jia, Y. Torigoshi, and Y. Shigesato, In situ analyses on negative ions in the indium-gallium-zinc oxide sputtering process, Appl. Phys. Lett. **103**, 013501 (2013).

[36] J. Serrano, A. H. Romero, F. J. Manjón, R. Lauck, M. Cardona, and A. Rubio, Pressure dependence of the lattice dynamics of ZnO: An *ab initio* approach, Phys. Rev. B **69**, 094306 (2004).

[37] S. Sarkar, O. Eriksson, D. D. Sarma, and I. Di Marco, Structural and electronic properties of the random alloy $ZnSe_xS_{1-x}$, Phys. Rev. B **105**, 184201 (2022).

[38] M. Feneberg and K. Thonke, Polarization fields of III-nitrides grown in different crystal orientations, J. Phys.: Condens. Matter **19**, 403201 (2007).

[39] Y. Ohashi, M. Arakawa, J. Kushibiki, B. M. Epelbaum, and A. Winnacker, Ultrasonic microspectroscopy characterization of AlN single crystals, Appl. Phys. Express **1**, 077004 (2008).

[40] H. K. Kim and M. Mathur, Structural and electrical properties of ZnO films deposited on GaAs substrates by RF magnetron sputtering, MRS Proc. **238**, 317 (1991).

[41] T. B. Bateman, Elastic moduli of single-crystal zinc oxide, J. Appl. Phys. **33**, 3309 (1962).

[42] M. A. Fraga, H. Furlan, R. S. Pessoa, and M. Massi, Wide bandgap semiconductor thin films for piezoelectric and piezoresistive MEMS sensors applied at high temperatures: An overview, Microsyst. Technol. **20**, 9 (2014).

[43] M. Mehedi Hassan, A. S. Ahmed, M. Chaman, W. Khan, A. H. Naqvi, and A. Azam, Structural and frequency dependent dielectric properties of Fe^{3+} doped ZnO nanoparticles, Mater. Res. Bull. **47**, 3952 (2012).

[44] C. Li, W. Guo, Y. Kong, and H. Gao, First-principles study of the dependence of ground-state structural properties on the dimensionality and size of ZnO nanostructures, Phys. Rev. B **76**, 035322 (2007).

[45] R. Ahuja, L. Fast, O. Eriksson, J. M. Wills, and B. Johansson, Elastic and high pressure properties of ZnO, J. Phys. Appl. **83**, 8065 (1998).

[46] F. Bernardini, V. Fiorentini, and D. Vanderbilt, Spontaneous polarization and piezoelectric constants of III–V nitrides, Phys. Rev. B **56**, R10024(R) (1997).

[47] P. Sharma, K. Kang, Y. Liu, B. Jang, J. Li, C. Yang, and J. Seidel, Optimizing the electromechanical response in morphotropic $BiFeO_3$, Nanotechnology **29**, 205703 (2018).

[48] M. Ahart, M. Somayazulu, R. E. Cohen, P. Ganesh, P. Dera, H.-K. Mao, R. J. Hemley, Y. Ren, P. Liermann, and Z. Wu, Origin of morphotropic phase boundaries in ferroelectrics, Nature (London) **451**, 545 (2008).

[49] A. M. Glazer, P. A. Thomas, K. Z. Baba-kishi, G. K. H. Pang, and C. W. Tai, Influence of short-range and long-range order on the evolution of the morphotropic phase boundary in $Pb(Zr_{1-x}Ti_x)O_3$, Phys. Rev. B **70**, 184123 (2004).

[50] F. D. Murnaghan, Finite elastic strain of cubic crystals, Am. J. Math. **59**, 235 (1937).

[51] F. Birch, The effect of pressure upon the elastic parameters of isotropic solids, according to Murnaghan's theory of finite strain, J. Appl. Phys. **9**, 279 (1938).

[52] F. Birch, Finite elastic strain of cubic crystals, Phys. Rev. **71**, 809 (1947).

[53] See Supplemental Material at http://link.aps.org/supplemental/10.1103/PhysRevB.109.134101 for additional information on the calculation results of (Mg,Zn)O critical transition pressure from the wurtzite to rocksalt phase, which includes Refs. [50–52,54,55,59–61].

[54] T. Katsura and Y. Tange, A simple derivation of the Birch-Murnaghan equations of state (EOSs) and comparison with EOSs derived from other definitions of finite strain, Minerals **9**, 745 (2019).

[55] K. Makiuchi, F. Kawamura, J. Jia, Y. Song, S. Yata, H. Tampo, H. Murata, and N. Yamada, Pressure-induced transition from wurtzite and epitaxial stabilization for thin films of rocksalt $MgSnN_2$, Chem. Mater. **35**, 2095 (2023).

[56] S. Desgreniers, High-density phases of ZnO: Structural and compressive parameters, Phys. Rev. B **58**, 14102 (1998).

[57] F. Decremps, J. Zhang, and R. C. Liebermann, New phase boundary and high-pressure thermoelasticity of ZnO, Europhys. Lett. **51**, 268 (2000).

[58] J. E. Jaffe, J. A. Snyder, Z. Lin, and A. C. Hess, LDA and GGA calculations for high-pressure phase transitions in ZnO and MgO, Phys. Rev. B **62**, 1660 (2000).

[59] H. Karzel, W. Potzel, M. Köfferlein, W. Schissl, M. Steiner, U. Hiller, G. M. Kalvius, D. W. Mitchell, T. P. Das, P. Blaha, K. Schwarz, and M. P. Pasternak, Lattice dynamics and hyperfine interactions in ZnO and ZnSe at high external pressures, Phys. Rev. B **53**, 11425 (1996).

[60] C. H. Bates, W. B. White, and R. Roy, New high-pressure polymorph of zinc oxide, Science **137**, 993 (1962).

[61] X. Yan, H. Dong, Y. Li, C. Lin, C. Park, D. He, and W. Yang, Phase transition induced strain in ZnO under high pressure, Sci. Rep. **6**, 24958 (2016).

[62] M. P. Molepo and D. P. Joubert, Computational study of the structural phases of ZnO, Phys. Rev. B **84**, 094110 (2011).

[63] B. Meyer and D. Marx, Density-functional study of the structure and stability of ZnO surfaces, Phys. Rev. B **67**, 035403 (2003).

[64] M. Kunisu, I. Tanaka, T. Yamamoto, T. Suga, and T. Mizoguchi, The formation of a rock-salt type ZnO thin film by low-level alloying with MgO, J. Phys.: Condens. Matter **16**, 3801 (2004).

[65] A. Seko, F. Oba, A. Kuwabara, and I. Tanaka, Pressure-induced phase transition in ZnO and ZnO-MgO pseudobinary system: A first-principles lattice dynamics study, Phys. Rev. B **72**, 024107 (2005).

[66] N. A. Hill and U. Waghmare, First-principles study of strain-electronic interplay in ZnO: Stress and temperature dependence of the piezoelectric constants, Phys. Rev. B **62**, 8802 (2000).

[67] S. Limpijumnong and W. R. L. Lambrecht, Theoretical study of the relative stability of wurtzite and rocksalt phases in MgO and GaN, Phys. Rev. B **63**, 104103 (2001).